

To appear in *The Astrophysical Journal*

## Estimating Black Hole Masses in Active Galactic Nuclei Using the Mg II $\lambda 2800$ Emission Line

Jian-Guo Wang<sup>1,2,5,6</sup>, Xiao-Bo Dong<sup>2,4</sup>, Ting-Gui Wang<sup>2,4</sup>, Luis C. Ho<sup>3</sup>, Weimin Yuan<sup>1</sup>, Huiyuan Wang<sup>2,4</sup>, Kai Zhang<sup>2,4</sup>, Shaohua Zhang<sup>2,4</sup>, and Hongyan Zhou<sup>2,4</sup>

### ABSTRACT

We investigate the relationship between the linewidths of broad Mg II  $\lambda 2800$  and  $H\beta$  in active galactic nuclei (AGNs) to refine them as tools to estimate black hole (BH) masses. We perform a detailed spectral analysis of a large sample of AGNs at intermediate redshifts selected from the Sloan Digital Sky Survey, along with a smaller sample of archival ultraviolet spectra for nearby sources monitored with reverberation mapping (RM). Careful attention is devoted to accurate spectral decomposition, especially in the treatment of narrow-line blending and Fe II contamination. We show that, contrary to popular belief, the velocity width of Mg II tends to be smaller than that of  $H\beta$ , suggesting that the two species are not cospatial in the broad-line region. Using these findings and recently updated BH mass measurements from RM, we present a new calibration of the empirical prescriptions for estimating virial BH masses for AGNs using the broad Mg II and  $H\beta$  lines. We show that the BH masses derived from our new formalisms show subtle but important differences compared to some of the mass estimators currently used in the literature.

*Subject headings:* black hole physics — galaxies: active — quasars: emission lines — quasars: general

<sup>1</sup>National Astronomical Observatories/Yunnan Observatory, Chinese Academy of Sciences, P.O. Box 110, Kunming, Yunnan 650011, China; wangjg, wmy@ynao.ac.cn

<sup>2</sup>Key Laboratory for Research in Galaxies and Cosmology, The University of Sciences and Technology of China, Chinese Academy of Sciences, Hefei, Anhui 230026, China; xbdong, twang@ustc.edu.cn

<sup>3</sup>The Observatories of the Carnegie Institution for Science, 813 Santa Barbara Street, Pasadena, CA 91101, USA; lho@obs.carnegiescience.edu

<sup>4</sup>Center for Astrophysics, University of Science and Technology of China, Hefei, Anhui 230026, China

<sup>5</sup>Department of Physics, Yunnan University, Kunming, Yunnan 650031, China

<sup>6</sup>Graduate School of the Chinese Academy of Sciences, 19A Yuquan Road, P.O. Box 3908, Beijing 100039, China

## 1. Introduction

It is generally accepted that active galactic nuclei (AGNs) are powered by the release of gravitational energy from material accreted onto supermassive black holes (BHs). The determination of BH mass ( $M_{\text{BH}}$ ) is crucial for understanding the AGN phenomena, the cosmological evolution of BHs, and even the coevolution of AGNs and their host galaxies. Yet, for such distant objects, it is currently impossible to obtain direct measurement of  $M_{\text{BH}}$  using spatially resolved stellar or gas kinematics. Fortunately, significant advances have been made in recent years from reverberation mapping (RM) studies of nearby Seyfert galaxies and quasi-stellar objects (QSOs; e.g., Wandel et al. 1999; Kaspi et al. 2000; Peterson et al. 2004). First, the anti-correlation between the radius of the broad-line region (BLR) and the velocity width of broad emission lines for single objects supports the idea that the BLR gas is virialized and that its velocity field is dominated by the gravity of the BH (Peterson & Wandel 1999, 2000; Onken & Peterson 2002). Second, the size of the BLR scales with the continuum luminosity (Kaspi et al. 2000, 2005), approximately as  $R \propto L^{0.5}$  (Bentz et al. 2006, 2009); the  $R-L$  relation offers a highly efficient procedure for estimating the BLR size without carrying out time-consuming RM observations. And third, the BH masses estimated by RM are roughly consistent (Gebhardt et al. 2000b; Ferrarese et al. 2001; Nelson et al. 2004; Onken et al. 2004) with the predictions from the tight correlation between  $M_{\text{BH}}$  and bulge stellar velocity dispersion established for inactive galaxies (the  $M_{\text{BH}}-\sigma_*$  relation; Gebhardt et al. 2000a; Ferrarese & Merritt 2000). These developments imply that we can estimate the BH mass in type 1 (broad-line, unobscured) AGNs by simple application of the virial theorem,  $M_{\text{BH}} = fRv^2/G$ , where  $f$  is a geometric factor of order unity that depends on the geometry and kinematics of the line-emitting region,  $R$  is the radius of the BLR derived from the AGN luminosity, and  $v$  is some measure of the virial velocity of the gas measured from single-epoch spectra. The feasibility of obtaining  $R$  and  $v$  from single-epoch spectra enables  $M_{\text{BH}}$  to be estimated very efficiently for large samples of AGNs, especially for luminous quasars at higher redshift that typically exhibit only slow and small-amplitude variability (e.g., Kaspi et al. 2007), with the assumption that the virial relation is independent of redshift and can be extrapolated to higher luminosities and masses. In practice, for those AGNs that have measurements of  $\sigma_*$ ,  $f$  is determined empirically by scaling the virial masses to the  $M_{\text{BH}}-\sigma_*$  relation of inactive galaxies (e.g., Onken et al. 2004). Implicit in this practice is the assumption—one open to debate (Greene & Ho 2006; Ho et al. 2008; Kim et al. 2008)—that active and inactive BHs should follow the same  $M_{\text{BH}}-\sigma_*$  relation. The most widely used estimator for  $v$  is the full width at half-maximum (FWHM) of the line.

Now, a large number of formalisms to estimate  $M_{\text{BH}}$  from single-epoch spectra have been proposed in the recent literature, using different broad emission lines optimized for different redshift regimes probed by (widely available) optical spectroscopy. At low redshifts, the lines of choice are H $\beta$  (Kaspi et al. 2000; Collin et al. 2006; Vestergaard & Peterson 2006) or H $\alpha$  (Greene &

(Ho 2005). At intermediate redshifts, Mg II  $\lambda 2800$  is used (McLure & Jarvis 2002), while at high redshifts, one has to resort to C IV  $\lambda 1549$  (Vestergaard 2002; Vestergaard & Peterson 2006). These formalisms are ultimately calibrated against RM masses based on the H $\beta$  BLR radius and linewidth measured from the variable (rms) spectra (Peterson et al. 2004). Because the H $\beta$  linewidth is typically smaller in the rms spectra than in the single-epoch or mean spectra (Vestergaard 2002; Collin et al. 2006; Sulentic et al. 2006), some authors have proposed that the FWHM used in the H $\beta$ -based formalisms should be further corrected to obtain unbiased  $M_{\text{BH}}$  estimates (Collin et al. 2006; Sulentic et al. 2006).

As for the Mg II-based formalisms, because there are very few RM experiments of the Mg II line, they are either based on the RM data for H $\beta$  (e.g., McLure & Jarvis 2002; McLure & Dunlop 2004) or calibrated against the H $\beta$  formalisms themselves (e.g., Kollmeier et al. 2006; Salviander et al. 2007). A strong, underlying assumption is that Mg II and H $\beta$  are emitted from the same location in the BLR and have the same linewidth (see also Onken & Kollmeier 2008). In support of this assumption, some authors find that Mg II and H $\beta$  indeed have very similar linewidths (e.g., McLure & Jarvis 2002; McLure & Dunlop 2004; Shen et al. 2008; also cf. Salviander et al. 2007). However, there are conflicting results in the literature: Corbett et al. (2003) claimed that Mg II is generally broader than H $\beta$ , whereas Dietrich & Hamann (2004) came to an opposite conclusion. Certainly, the most direct way to settle this issue is through direct RM of the Mg II line. So far there are only two objects that have successful Mg II RM, NGC 5548 (Clavel et al. 1991; Dietrich & Kollatschny 1995) and NGC 4151 (Metzroth et al. 2006). These studies tentatively suggest that Mg II responds more slowly to continuum variations than H $\beta$ , implying that the Mg II-emitting region is larger than that radiating H $\beta$ .

Thus, there are still some important open questions regarding the robustness of  $M_{\text{BH}}$  measurements based on Mg II. What is the relation between the linewidths of H $\beta$  and Mg II? Are estimates of  $M_{\text{BH}}$  based on Mg II consistent with those based on H $\beta$ ? These basic questions are critical for understanding the systematic uncertainties in studies of the cosmological evolution of BHs (cf. Shen et al. 2008; McGill et al. 2008; Denney et al. 2009a). To address the above questions, we perform a detailed comparison of the widths of the Mg II and H $\beta$  lines using single-epoch spectra for a large, homogeneous sample of Seyfert 1 nuclei and QSOs at intermediate redshifts culled from the Sloan Digital Sky Survey (SDSS; York et al. 2000). We further compare single-epoch Mg II linewidths with H $\beta$  linewidths measured from the rms spectra of AGNs with RM observations, finding systematic deviations between the two. We present a recalibration of the Mg II virial mass estimator and compare our formalism with previous ones in the literature.

This paper adopts the following set of cosmological parameters:  $H_0=70 \text{ km s}^{-1} \text{ Mpc}^{-1}$ ,  $\Omega_m=0.3$ , and  $\Omega_\Lambda=0.7$ .

## 2. Sample and Data Analysis

### 2.1. The Samples

The sample of best-studied H $\beta$  emission lines is the one compiled by Peterson et al. (2004) for RM studies of 35 low-redshift AGNs. To compare H $\beta$  and Mg II for this sample, we located usable ultraviolet (UV) spectra for 29 sources, 16 from the *Hubble Space Telescope* (*HST*) and 13 from the *International Ultraviolet Explorer* (*IUE*) data archives. This sample will be used to study the relationship between single-epoch Mg II linewidths and H $\beta$  linewidths measured from rms spectra, and to fit a new  $M_{\text{BH}}$  formalism based on single-epoch Mg II.

We also selected Seyfert 1 galaxies and QSOs in the redshift range  $0.45 < z < 0.75$  from the Fifth Data Release (DR5) of the SDSS spectroscopic database (Adelman-McCarthy et al. 2007). Within this redshift range, both H $\beta$  and Mg II lie within the SDSS spectral coverage. To ensure accurate measurement of both lines, we only select objects with a mean signal-to-noise ratio (S/N)  $\geq 20$  per pixel in both the H $\beta$  (4600–5100 Å) and the Mg II (2700–2900 Å) regions. We discarded 26 spectra that have either broad absorption lines or too many narrow absorption lines, or for which the H $\beta$  or the Mg II regions were corrupted by bad pixels. The remaining 495 objects have spectra that can be well fitted, as confirmed by visual inspection. This sample will be used to investigate the FWHM relation between Mg II and H $\beta$  in single-epoch spectra and to compare our Mg II formalism with others in the literature.

### 2.2. Spectral Fitting

The spectra are first corrected for Galactic extinction using the extinction map of Schlegel et al. (1998) and the reddening curve of Fitzpatrick (1999). Then the spectra are fitted using an IDL code based on MPFIT (Markwardt 2009), which performs  $\chi^2$ -minimization by the Levenberg–Marquardt technique. Bad data are masked during the fitting.

To measure the H $\beta$  line, we perform continuum subtraction and emission-line fitting following the method described in detail in Dong et al. (2008). We first fit simultaneously the featureless nonstellar continuum (assumed to be a power law), the Fe II multiplet emission, and other emission lines in the wavelength range 4200–5600 Å, giving emphasis on the proper determination of the local pseudocontinuum (continuum + Fe II emission). For spectra with fits having a reduced  $\chi^2 > 1.1$  around H $\beta$  (4750–5050 Å), a refined fit of the emission-line profiles is performed to the pseudocontinuum-subtracted spectra using the code described in Dong et al. (2005). Each line of the [O III]  $\lambda\lambda 4959, 5007$  doublet is modeled with two Gaussians, one accounting for the line core and the other for a possible blue wing as seen in many objects. The doublet lines are assumed to

have the same redshifts and profiles, and the flux ratio  $\lambda 5007/\lambda 4959$  is fixed to the theoretical value of 3. The narrow component of  $H\beta$  is fitted with one Gaussian, assumed to have the same width as the line core of [O III]  $\lambda 5007$ . The broad component of  $H\beta$  is fitted with as many Gaussians as statistically justified (see Dong et al. 2008 for details).

To measure the Mg II line, we adopt the following procedure. We first obtain an initial estimate of the nonstellar featureless continuum by fitting a simple power law,

$$f^{\text{PL}}(\lambda; a, \beta) = a \left( \frac{\lambda}{2200} \right)^{\beta}, \quad (1)$$

to the data in several continuum windows near 2200, 3000, 4000, and 4200 Å that suffer little from emission-line contamination, if available. Then, the power-law local continuum, a Balmer continuum, and an Fe II emission template, which together constitute the so-called pseudocontinuum, are fitted simultaneously. The fitting is performed in the restframe wavelength range 2200–3500 Å, if available, with the small region contaminated significantly by Mg II masked out. The fitting range is set by the wavelength coverage of the UV Fe II template,  $f^{\text{T06}}(\lambda)$ , which was generated by Tsuzuki et al. (2006) based on their measurements of I Zw 1. In the wavelength region covered by Mg II emission, they employed a semi-empirical iteration procedure to build the template. They first generated a theoretical Fe II model spectrum with the photoionization code CLOUDY (Ferland et al. 1998) and subtracted it from the observed I Zw 1 spectrum around Mg II. Then the Mg II doublet was fit assuming each line has the same profile as  $H\alpha$ . And finally they obtained the Fe II template underneath Mg II by subtracting the Mg II fit from the observed spectrum. To match the linewidth and possible velocity shift of Fe II lines, we build the Fe II model by convolving the I ZW 1 template with a Gaussian of width  $\sigma_g$  and shifting it with a velocity  $v_{\text{shift}}$  in logarithmic wavelength space (i.e., the velocity space because  $d \ln \lambda = d\lambda/\lambda = v/c$ ), as follows,

$$f^{\text{FeII}}(\lambda; c, v_{\text{shift}}, \sigma_g) = c f^{\text{T06}}(\lambda, v_{\text{shift}}) \otimes G(\lambda, \sigma_g). \quad (2)$$

As in Dietrich et al. (2002), the Balmer continuum is assumed to be produced in partially optically thick clouds with a uniform temperature,<sup>1</sup>

$$f^{\text{BaC}}(\lambda; d, T_e, \tau_{\lambda}) = d B_{\lambda}(T_e)(1 - e^{-\tau_{\lambda}}); \quad \lambda \leq \lambda_{\text{BE}} \quad (3)$$

$$\tau_{\lambda} = \tau_{\text{BE}} \left( \frac{\lambda}{\lambda_{\text{BE}}} \right)^3, \quad (4)$$

---

<sup>1</sup>We do not account for the velocity broadening of the Balmer continuum, because the Balmer continuum in our fitting range is insensitive to this effect.

where  $\lambda_{\text{BE}} = 3646 \text{ \AA}$  (3.4 eV),  $\tau_{\text{BE}}$  is the optical depth at  $\lambda_{\text{BE}}$ , and  $B_\lambda(\lambda, T_e)$  is the Planck blackbody spectrum at the electron temperature  $T_e$ .

To sum up, the full model for the pseudocontinuum is as follows:

$$f(\lambda) = f^{\text{PL}}(\lambda; a, \beta) + f^{\text{Fe II}}(\lambda; c, v_{\text{shift}}, \sigma_g) + f^{\text{BaC}}(\lambda; d, T_e, \tau_{\text{BE}}) . \quad (5)$$

The fitting is performed in logarithmic wavelength space. During the fitting, the normalization  $a$  and slope  $\beta$  of the power-law continuum, the normalization  $c$ , velocity shift  $v_{\text{shift}}$  and broadening velocity  $\sigma_g$  of the Fe II emission, and the parameters  $d$ ,  $T_e$ , and  $\tau_{\text{BE}}$  of the Balmer continuum are set to be free parameters.

We note that in the fitting range of 2200–3500 Å the Balmer continuum is hard to be constrained and separated from the power-law continuum and Fe II emission (cf. Figure 8 of Tsuzuki et al. 2006). In this work, we are not concerned with the properties of the Balmer continuum, but with the proper separation of the power-law continuum, Fe II, and Mg II. To minimize the effect of the possible poor fitting of Balmer continuum on the determination of the power-law continuum, Fe II, and Mg II, we constrain the power-law continuum parameters in such a way that they vary only around the best-fit values obtained from the first step, by a factor of < 10% for the normalization  $a$  and < 20% for the slope  $\beta$ . During this step, we assign additionally larger weights to the regions 2400–2650 Å and 2920–2990 Å in order to improve the fit for the Fe II emission surrounding Mg II (cf. Section 2.3 of Dong et al. 2008).

Once the pseudocontinuum is fitted and subtracted, the Mg II emission line is fitted in the range of 2700–2900 Å, if available. For the SDSS sample, there are a few cases where a small number of narrow absorption lines are present around the Mg II emission line. To further eliminate the absorption lines in these objects, we first fit the Mg II emission line with one Gaussian, and then mask those pixels of absorption features deviating strongly from the model. The Mg II line is fitted in the following way. Each of the two Mg II  $\lambda\lambda 2796, 2803$  doublet lines is modeled with two components, one broad and the other narrow. The broad component is a truncated five-parameter Gauss–Hermite series (van der Marel & Franx 1993; see also Salviander et al. 2007); the narrow component is a single Gaussian. The broad components of the doublet lines are set to have the same profile, with the flux ratio  $\lambda 2796/\lambda 2803$  set to be between 2:1 and 1:1 (Laor et al. 1997), and the doublet separation set to the laboratory value. The same prescription is applied to the narrow components, with the following additional constraints:  $\text{FWHM} \leq 900 \text{ km s}^{-1}$  and flux < 10% of the total Mg II flux (Wills et al. 1993; see also McLure & Dunlop 2004). The fitting results for all the 495 objects are reasonable according to our visual inspection finally. The FWHM value is measured from the Gauss–Hermite model of Mg II  $\lambda 2796$ . The monochromatic flux of the continuum is measured from the fitted power law.

There are several other emission lines in the fitting region, identified from the composite

SDSS QSO spectrum (see Table 2 of Vanden Berk et al. 2001); yet, because of their weakness, we simply masked them out in the fit. Because of the limited wavelength coverage of the RM sample, we cannot separate the Balmer continuum from the power-law continuum. Thus, the Balmer continuum was not included in the fits for this sample. Additionally, there are deep narrow absorption features around Mg II in the spectra of NGC 3227, NGC 3516, NGC 3783, and NGC 4151 in the RM sample. Each of the absorption features is fitted simultaneously with a Gaussian when fitting the Mg II emission line.

We estimate the measurement uncertainties of the parameters using the bootstrap method<sup>2</sup> described in Dong et al. (2008, Section 2.5). The estimated  $1\sigma$  errors for the broad-line fluxes are typically 10% for Mg II and 8% for H $\beta$ , while the errors on the broad-line FWHM are  $\sim$ 20% for Mg II and  $\sim$ 15% for H $\beta$ . The power-law continua have uncertainties of 8% for the slope and 5% for the normalization. The above discussion does not account for possible systematic errors resulting from the subtraction of the continuum or our treatment of the Fe II and narrow lines.

Figure 1 shows two examples of the fits. The continuum and emission-line parameters for the RM and SDSS samples are listed in Tables 1 and 2, respectively. The data and fitting parameters are available online for the decomposed spectral components (continuum, Fe II, and other emission lines). <sup>3</sup>

### 2.3. Regression Methods

In the next section, we will fit the linewidth relations and BH mass estimators using several regression methods. The purpose of using these different methods is for ease of comparison with results in the literature, and to investigate possible differences in the fitting results caused by the different methods. Here we briefly summarize the regression methods used.

---

<sup>2</sup>To estimate the errors on the fitted parameters, we generate 500 spectra by randomly combining the scaled model emission lines of one object (denoted as “A”) to the emission-line subtracted spectrum of another object (denoted as “B”). The emission-line model of object “A” is scaled in such a way that it has the same broad Mg II flux as object “B,” in order to minimize changes in S/N within the emission-line spectral regions in the simulated spectra. Then, we fit the simulated spectra following the same procedure as described in Section 2.2. For each parameter, we consider the error typical of our sample to be the standard deviation of the relative difference between the input and the recovered parameter values. These relative differences turn out to be normally distributed for each of the parameters concerned.

<sup>3</sup>Available at [http://staff.ustc.edu.cn/~xbdong/Data\\_Release/MgII\\_Hbeta/](http://staff.ustc.edu.cn/~xbdong/Data_Release/MgII_Hbeta/), together with auxiliary code to explain the parameters and to demonstrate the fitting.

1. Ordinary least-squares (OLS), which is a least-squares regression method without considering measurement errors.
2. Weighted least-squares (WLS), which takes into account only measurement uncertainties in the dependent variable.
3. FITexy (Press et al. 1992), which numerically solves for the minimum orthogonal  $\chi^2$  using an interactive root-finding algorithm. It accounts for measurement uncertainties in both coordinates, but does not account for intrinsic scatter.
4. FITexy\_T02, the version of FITexy modified by Tremaine et al. (2002), accounts for possible intrinsic scatter in the dependent variable by adding in quadrature a constant to the error value so as to obtain a reduced  $\chi^2$  of 1.
5. Gaussfit (McArthur et al. 1994), which implements generalized least-squares using the robust Householder Orthogonal Transformations (Jefferys 1980, 1981). It can handle errors in both coordinates, but does not account for intrinsic scatter.
6. The bivariate correlated errors and intrinsic scatter (BCES) regression method (Akritas & Bershady 1996), which accounts for measurement errors on both coordinates in the fit using bivariate correlated errors, and possible intrinsic scatter (but does not output any quantification of this scatter). The results of the two symmetrical versions, bisector and orthogonal, are used in this paper.
7. LINMIX\_ERR (Kelly 2007), which accounts for measurement errors, nondetections, and intrinsic scatter by adopting a Bayesian approach to compute the posterior probability distribution of parameters, given observed data. We also consider the multivariate extension, MLINMIX\_ERR.

As we find below, most of the above regression methods give consistent results. For the linewidth-linewidth relationships, since there is no prior knowledge about which variable is independent and which is dependent, we adopt the results given by the BCES orthogonal method, which treats both variables symmetrically. For the BH mass scaling relations, we adopt formally the results given by the LINMIX\_ERR method, since it is argued to be among the most robust regression methods with the possibility of reliable estimation of intrinsic dispersion (Kelly 2007).

For some of the regression methods listed above no intrinsic scatter ( $\sigma_{\text{int}}$ ) can be inferred. We can give a rough yet simple estimate of  $\sigma_{\text{int}}^2$  by deducting the contribution of the measurement errors from the variance in the regression residuals ( $\sigma_{\text{tot}}^2$ ), by using an approximate relation  $\sigma_{\text{int}}^2 = \sigma_{\text{tot}}^2 - \langle \sigma_m \rangle^2$ , where  $\langle \sigma_m \rangle$  is the median of the total measurement errors computed from  $\sigma_m = \sigma_y + \text{slope} * \sigma_x$ . If  $\sigma_{\text{tot}}$  is smaller than  $\langle \sigma_m \rangle$ ,  $\sigma_{\text{int}}$  was set to be 0. As a check, this rough estimate

can be compared with the intrinsic scatter given by some of the regression methods that provide such a measure.

### 3. Results

The main motivation of this work is to investigate whether reliable BH masses can be estimated using the Mg II linewidth as a virial velocity indicator. Linewidths are commonly parameterized as FWHM, or sometimes as  $\sigma_{\text{line}}$ —the line dispersion or second moment of the line profile (Peterson et al. 2004). Both quantities have intrinsic strengths and weaknesses (see Section 3 of Peterson et al. 2004). Collin et al. (2006), in particular, argued that the use of FWHM rather than  $\sigma_{\text{line}}$  introduces systematic bias in  $M_{\text{BH}}$  estimates. Although  $\sigma_{\text{line}}$  is a better tracer of virial velocity than FWHM in rms spectra (Peterson et al. 2004), the line dispersion is very sensitive to measurement errors in the line wings, making it especially susceptible to inaccuracies caused by deblending and subtraction of Fe II and other emission lines, effects that are particularly significant in mean and single-epoch spectra. By contrast, the FWHM is less prone to these effects; it is more sensitive to corrections for the narrow-line component, which, fortunately, is quite weak for Mg II (see Section 4.1). In this work, we opt to use the FWHM to parameterize the linewidth.

#### 3.1. Single-epoch Mg II FWHM versus H $\beta$ FWHM

We first investigate the relation between the FWHM of Mg II and H $\beta$ , using single-epoch data from our SDSS sample. The relation is illustrated in Figure 2. A strong correlation is present, but apparently deviates from one-to-one. This trend has been noticed in the literature, but it was less prominent because of the narrower dynamical range in velocity covered in previous studies (e.g., Salviander et al. 2007; Hu et al. 2008). With our high-quality data, we can now fit a strict relation. We perform a linear regression in log–log space using the methods described in Section 2.3; the results are listed in Table 3. As can be seen, most of the methods give mutually consistent results. For our subsequent analysis, we adopt the BCES (orthogonal) method because it treats both variables symmetrically (Section 2.3). We find

$$\log \left[ \frac{\text{FWHM}(\text{Mg II})}{1000 \text{ km s}^{-1}} \right] = (0.81 \pm 0.02) \log \left[ \frac{\text{FWHM}(\text{H}\beta)}{1000 \text{ km s}^{-1}} \right] + (0.05 \pm 0.01). \quad (6)$$

This means that *the line-emitting locations of H $\beta$  and Mg II in the BLR are not identical*. If they were, we would expect a linear relation between the two, with no offset. The intrinsic scatter of

this relation, as given by the regression methods listed above, is extremely small and negligible compared to the measurement errors. The latter is actually comparable to the *total* scatter ( $\sigma_{\text{tot}}$ ) of the relationship, which is found to be 0.08 dex.

### 3.2. Single-epoch Mg II FWHM versus rms H $\beta$ $\sigma_{\text{line}}$

Since the assumption that Mg II FWHM is identical to H $\beta$  FWHM does not hold, we explore the relation between Mg II FWHM and rms H $\beta$   $\sigma_{\text{line}}$ , which has been argued to be a good tracer of the virial velocity of the BLR clouds emitting (variable) H $\beta$  (see references in Section 1). We use data for the 29 objects in the RM sample that have UV spectra to perform this exploration. Mg II FWHM is measured from the single-epoch *HST/IUE* spectra, as listed in Table 1. The data for rms H $\beta$   $\sigma_{\text{line}}$  are mainly taken from Peterson et al. (2004). In addition, we use updated RM data for NGC 4051 (Denney et al. 2009b), NGC 4151 (Metzroth et al. 2006), NGC 4593 (Denney et al. 2006), NGC 5548 (Bentz et al. 2007), and PG 2130+099 (Grier et al. 2008). For objects with multiple measurements, the geometric mean (i.e., the mean in the log scale) was used.

We find that the slope of the relation between Mg II FWHM and rms H $\beta$   $\sigma_{\text{line}}$  deviates from unity, with a best fit of

$$\log \left[ \frac{\sigma_{\text{line}}(\text{H}\beta, \text{rms})}{1000 \text{ km s}^{-1}} \right] = (0.85 \pm 0.21) \log \left[ \frac{\text{FWHM}(\text{Mg II})}{1000 \text{ km s}^{-1}} \right] - (0.21 \pm 0.12) . \quad (7)$$

The formal relation is nonlinear although the significance level is only about 1  $\sigma$ . A nonlinear relation between Mg II FWHM and rms H $\beta$   $\sigma_{\text{line}}$  is not very surprising, in light of a similar situation observed for H $\beta$  FWHM (Collin et al. 2006; also Sulentic et al. 2006, Section 1). For verification, we also fit the relation between H $\beta$  FWHM in the mean spectra and rms H $\beta$   $\sigma_{\text{line}}$  using data for 35 objects in the RM sample; the FWHM data are taken from Collin et al. (2006) and from the updated sources mentioned above. The best-fit relation deviates from unity even more seriously than the case of Mg II FWHM:

$$\log \left[ \frac{\sigma_{\text{line}}(\text{H}\beta, \text{rms})}{1000 \text{ km s}^{-1}} \right] = (0.54 \pm 0.08) \log \left[ \frac{\text{FWHM}(\text{H}\beta, \text{mean})}{1000 \text{ km s}^{-1}} \right] - (0.09 \pm 0.05) . \quad (8)$$

These relations between rms H $\beta$   $\sigma_{\text{line}}$  and Mg II and H $\beta$  FWHM are illustrated in Figure 3. The total 1  $\sigma$  scatter around these relationships is  $\sigma_{\text{tot}} = 0.12$  dex for Equation (7) and 0.09 dex for

Equation (8). Given the relatively small measurement errors of the linewidths, there likely exists intrinsic scatter in these relationships. Using the simple method of deducting the measurement errors from the total scatter, as described in Section 2.3, we find  $\sigma_{\text{int}} \approx 0.09$  dex and  $\approx 0.08$  dex for the relationships of Equations (7) and (8), respectively. The underlying reason for the nonlinearity of these relationships may be, at least partially, that the  $\sigma_{\text{line}}$  of rms spectra traces the velocity of the line-emitting region that responds to continuum variation, while the FWHM of single-epoch spectra may be contributed by various components (see Section 4.2 for a discussion).

### 3.3. Practical Formalism for New Mg II-based $M_{\text{BH}}$ Estimator

As described above, Mg II FWHM is not identical to, but rather generally smaller than, H $\beta$  FWHM; for Mg II FWHM  $\gtrsim 6000$  km s $^{-1}$ , the difference is  $\gtrsim 0.2$  dex. This means that one of the fundamental premises of the previous Mg II-based formalisms—that Mg II and H $\beta$  trace similar kinematics—does not hold. Moreover, similar to the behavior of H $\beta$  FWHM, Mg II FWHM seems not to be linearly proportional to rms H $\beta$   $\sigma_{\text{line}}$ . If rms  $\sigma_{\text{line}}$  is more directly linked to the virial velocity, this implies that we cannot build a virial  $M_{\text{BH}}$  formalism by simply assuming  $M_{\text{BH}} \propto \text{FWHM}^2$ . Furthermore, the  $M_{\text{BH}}$  data of the RM AGNs used in McLure & Jarvis (2002) and McLure & Dunlop (2004) have since been recalibrated or updated (Peterson et al. 2004; Denney et al. 2006, 2009b; Metzroth et al. 2006; Bentz et al. 2007; Grier et al. 2008). Thus, it is necessary to reformulate the virial  $M_{\text{BH}}$  formalism based on single-epoch Mg II FWHM.

We proceed by assuming that there is a tight relation between the BLR radius of the Mg II-emitting region and the AGN continuum luminosity, in the form  $R_{\text{Mg II}} \propto L^\beta$ , and another between the virial velocity of Mg II and the FWHM of the line, in the form  $v_{\text{virial}}^2 \propto \text{FWHM}^\gamma$ . Then, using the 29 objects with the  $M_{\text{BH}}$  values based on RM and the Mg II data measured here (Table 1), we calculate the free parameters by fitting

$$\log \left[ \frac{M_{\text{BH}}(\text{RM})}{10^6 M_\odot} \right] = a + \beta \log \left( \frac{L_{3000}}{10^{44} \text{ erg s}^{-1}} \right) + \gamma \log \left[ \frac{\text{FWHM}(\text{Mg II})}{1000 \text{ km s}^{-1}} \right], \quad (9)$$

where  $L_{3000} \equiv \lambda L_\lambda(3000 \text{ \AA})$ . The RM-based  $M_{\text{BH}}$  data are mainly taken from Peterson et al. (2004), who calibrated the  $f$ -factor by normalizing to the  $M_{\text{BH}}-\sigma_*$  relation of Onken et al. (2004);  $M_{\text{BH}}$  for the updated objects comes from the references given in Section 3.2.

We fit Equation (9) following four schemes, using the (LINMIX\_ERR/MLINMIX\_ERR) method of Kelly (2007):

1.  $a$ ,  $\beta$ , and  $\gamma$  are treated as free parameters.
2.  $a$  and  $\beta$  are treated as free parameters, but, as in all previous formalisms, we fix  $\gamma = 2$ .
3.  $a$  and  $\beta$  are treated as free parameters, but we set  $\gamma = 1.70$ , as suggested by Equation (7).
4.  $a$  and  $\gamma$  are treated as free parameters, but we fix  $\beta = 0.5$ , as suggested by the latest  $R-L$  relation (Bentz et al. 2006, 2009).

Table 4 lists the best-fit regression for each scheme (Columns 1–4), as well as comparisons between the  $M_{\text{BH}}$  estimates based on each scheme and the RM-based masses (Column 5). It is apparent that the best-fit values for  $\beta$  for all the schemes are consistent with 0.5 within  $1\sigma$  error. Interestingly,  $\gamma$  appears to be marginally smaller than 2, since the standard deviation of the BH mass for Scheme 2 is slightly larger than that for the other three schemes. If we set  $\beta = 0.5$  (i.e., adopt Scheme 4), the best-fit Mg II-based formalism is

$$\begin{aligned} \log \left( \frac{M_{\text{BH}}}{10^6 M_{\odot}} \right) &= (1.13 \pm 0.27) + 0.5 \log \left( \frac{L_{3000}}{10^{44} \text{ erg s}^{-1}} \right) \\ &\quad + (1.51 \pm 0.49) \log \left[ \frac{\text{FWHM(Mg II)}}{1000 \text{ km s}^{-1}} \right] . \end{aligned} \quad (10)$$

Fitting the  $H\beta$  FWHM data for the 35 RM objects under the same assumptions ( $\beta = 0.5$ ), the  $H\beta$ -based formalism becomes

$$\begin{aligned} \log \left( \frac{M_{\text{BH}}}{10^6 M_{\odot}} \right) &= (1.39 \pm 0.14) + 0.5 \log \left( \frac{L_{5100}}{10^{44} \text{ erg s}^{-1}} \right) \\ &\quad + (1.09 \pm 0.23) \log \left[ \frac{\text{FWHM}(H\beta)}{1000 \text{ km s}^{-1}} \right] . \end{aligned} \quad (11)$$

The best-fitting  $\gamma = 1.09 \pm 0.23$  agrees well with the  $\sigma_{\text{line}}(H\beta, \text{rms}) - \text{FWHM}(H\beta)$  relation derived in Equation (8).

Comparisons between the RM-based masses and the  $M_{\text{BH}}$  estimates from our new  $M_{\text{BH}}$  formalisms using Mg II FWHM (Equation (10)) and  $H\beta$  FWHM (Equation (11)) are illustrated in Figure 4. Following Vestergaard & Peterson (2006), we calculate the deviation of the new calibrated single-epoch  $M_{\text{BH}}$  estimates from the RM-based masses,  $\Delta M_{\text{BH}}(\text{RM})$ . The mean of the deviations,  $\langle \Delta M_{\text{BH}}(\text{RM}) \rangle$ , is only 0.01 dex for our Mg II estimator, and the  $1\sigma$  scatter is 0.4 dex (Column 5 in Table 4). As a comparison, if we use the formalism of McLure & Dunlop (2004),

the deviations from the same RM-based masses have a mean of 0.38 dex and a  $1\sigma$  scatter of 0.45 dex. For our  $H\beta$  estimator,  $\langle \Delta M_{BH}(\text{RM}) \rangle$  is 0.01 dex and the  $1\sigma$  scatter is 0.3 dex, compared to  $\langle \Delta M_{BH}(\text{RM}) \rangle = 0.05$  dex and  $\sigma = 0.4$  dex if the formalism of Vestergaard & Peterson (2006) is used.<sup>4</sup> It should be noted that these scatters of the scaling relations, which give a measure of the uncertainty in estimating  $M_{BH}$  from the single-epoch spectroscopic data, is relative to the RM-based masses only. Since, as pointed out by Vestergaard & Peterson (2006), the RM-based masses themselves are uncertain typically by a factor of  $\sim 2.9$  (as calibrated against the  $M_{BH}-\sigma_*$  relation; Onken et al. 2004), the absolute uncertainty of the masses thus estimated is even higher. For the  $H\beta$  formalism, we find this absolute uncertainty to be a factor of  $\sim 3.5$ , to be compared with a factor of  $\sim 4$  given in Vestergaard & Peterson (2006); for Mg II, we estimate that the absolute uncertainty is a factor of  $\sim 4$ .

As shown above, our new formalisms improve somewhat the scatter in the single-epoch  $M_{BH}$  estimates compared to previous  $H\beta$  and Mg II estimators, by 0.1 dex and 0.05 dex, respectively. Given the same linewidth and luminosity data used in this work and in Vestergaard & Peterson (2006), the reduction in the scatter of the  $M_{BH}$  estimates should result from a decrease in the *intrinsic* dispersion of our improved single-epoch  $M_{BH}$  formalisms. Using the LINMIX\_ERR method, the intrinsic scatter inherent in our  $M_{BH}$  formalism can be inferred to be 0.08 dex ( $1\sigma$ ) for the  $H\beta$  and 0.14 dex for Mg II.

Figure 5 compares our new Mg II-based formalism (we show only Schemes 2 and 4) with the previous  $H\beta$ -based formalisms of Vestergaard & Peterson (2006; panel a) and Collin et al. (2006; panel b), as well as our newly derived version using the SDSS sample of 495 Seyfert 1s and QSOs (Equation (11); panel c). The  $M_{BH}$  residuals between our Mg II formalism and the  $H\beta$  formalisms are listed in Table 4 (Columns 6–8). While our Mg II-based formalism, especially for Scheme 4 (Equation (10)), agrees well with our  $H\beta$ -based formalism (Equation (11)), note that it deviates markedly from the  $H\beta$  formalism of Vestergaard & Peterson. This confirms previous suspicions (Collin et al. 2006; Sulentic et al. 2006) that the use of  $H\beta$  FWHM from mean and single-epoch spectra with the assumption  $\gamma = 2$  introduces systematic bias into  $M_{BH}$  estimates.

We further compare our new Mg II-based formalism (Equation (10)) with other Mg II formalisms widely used in the literature. Figure 5 illustrates that the  $M_{BH}$  estimates following the formalisms of McLure & Dunlop (2004; panel d), Kollmeier et al. (2006; panel e), and Salviander et al. (2007; panel f) show large systematic deviations, mostly in the sense of being smaller than ours. The deviations stem primarily from the recalibration of the RM masses; other factors are

---

<sup>4</sup> It should be noted that here we use the averaged spectrum for an object with more than one observation, unlike in Vestergaard & Peterson (2006) where the individual single-epoch  $H\beta$  spectral data were used in the regression. If we take the latter approach, our  $H\beta$  estimator gives a  $\langle \Delta M_{BH}(\text{RM}) \rangle = -0.07$  dex and a scatter of 0.33 dex, while Vestergaard & Peterson (2006) gave  $\langle \Delta M_{BH}(\text{RM}) \rangle = -0.12$  dex and a scatter of 0.45 dex.

discussed in Section 4.3. We note that a yet-unpublished Mg II-based formalism by M. Vestergaard et al. (in preparation) used in the recent literature (e.g., Kelly et al. 2009) is almost identical to our Scheme 2 (with  $\gamma$  fixed to 2).

## 4. Discussion

### 4.1. Testing the Effect of Narrow-line Subtraction

The narrow component of Mg II is generally weak in luminous type 1 AGNs (e.g., Wills et al. 1993; Laor et al. 1994), and so its contribution to the total line flux can be safely neglected. However, its presence might have a more pronounced impact on the FWHM measurement of broad Mg II. In the literature, narrow Mg II was accounted for in the line fitting by some authors (e.g., McLure & Dunlop 2004), but not by others (e.g., Salviander et al. 2007). As there is usually no clear inflection in the Mg II profile, separating narrow Mg II from the broad component is often challenging. Fortunately, for the spectra in our SDSS sample, [O III]  $\lambda 5007$  is present, and thus we can use [O III] to try to constrain narrow Mg II, to test the effect of narrow Mg II on the FWHM measurement of broad Mg II, and also to test the reliability of our Mg II fitting strategy.

In addition to the default fitting strategy described in Section 2.2, in which narrow Mg II is modeled as a single free Gaussian, we tried two alternative strategies in which narrow Mg II is (A) not fit at all, and (B) is fit using a single-Gaussian model constrained to that of the line core of [O III]. Broad Mg II is modeled as described in Section 2.2. We find that, for the 495 objects in our SDSS sample, the distributions of the reduced  $\chi^2$  of the Mg II emission line fit of the three approaches can be approximated reasonably well with a log-normal function. The peak and standard deviation of the reduced  $\chi^2$  are very similar for all three, being (0.97, 0.10 dex) for the default strategy, (1.01, 0.10 dex) for Strategy A, and (0.99, 0.10 dex) for Strategy B. Regarding the FWHM of broad Mg II, the mean and standard deviation are ( $-0.04$ , 0.05) for  $\log[\frac{\text{FWHM(A)}}{\text{FWHM(default)}}]$  and (0.00, 0.05) for  $\log[\frac{\text{FWHM(B)}}{\text{FWHM(default)}}]$ . For Strategy B, the fitted flux of narrow Mg II is less than 10% of the total line flux for almost all the objects. Our tests show that omitting the subtraction of narrow Mg II has a negligible effect on the FWHM of broad Mg II, typically decreasing it only by a tiny factor of 0.04 dex. We further confirm that our default procedure for modeling narrow Mg II is consistent with that using the [O III] core as a template.

The above Strategy A is exactly the same as the Mg II-fitting method adopted by Salviander et al. (2007). We also compared our method with that of McLure & Dunlop (2004). When fitting the spectra in our SDSS sample by the method of McLure & Dunlop (2004), on average the FWHM of broad Mg II is larger than that of our method by 0.1 dex.

#### 4.2. $M_{\text{BH}}$ Estimators with Single-epoch H $\beta$ and Mg II

As analyzed in detail by Sulentic et al. (2006), the overall profile of the H $\beta$  emission line, as viewed in single-epoch spectra, likely comprises multiple components emitted from different sites. First, as a recombination line, H $\beta$  can arise from BLR gas that is very close to the central engine. Then H $\beta$  can be gravitationally redshifted, as (part of) the component of the “very BLR” (Marziani & Sulentic 1993). Such clouds may be optically thin to the ionizing continuum, such that H $\beta$  is no longer responsive to continuum variation (Shields et al. 1995). Second, like C IV  $\lambda$ 1549, H $\beta$  can be produced partly in high-ionization winds, as some observations suggest (see Marziani et al. 2008, and references therein). This wind component would not be virial. Third, H $\beta$  can also be produced on the surface of the accretion disk, both by recombination and collisional excitation (Chen & Halpern 1989; Wang et al. 2005; Wu et al. 2008); this component would be highly anisotropic (cf. Collin et al. 2006). Considering the above factors, it is not surprising that single-epoch FWHM is not linearly proportional to  $\sigma_{\text{line}}$  for rms H $\beta$  (Equation (8)).

Mg II, as a low-ionization, collisionally excited emission line, cannot be produced in clouds very close to the central engine. Furthermore, because Mg II originates only from optically thick clouds, radiation pressure force cannot act on them very significantly (cf. Marconi et al. 2008, 2009; Dong et al. 2009a,b), and thus Mg II suffers little from nonvirial motion. Hence, compared to H $\beta$ , the FWHM of single-epoch Mg II should, in principle, deviate less, if at all, from the true virial velocity of the line-emitting clouds. This is suggested by the best-fit value for  $\gamma$  in Equation (10), which indicates  $v_{\text{virial}}^2 \propto \text{FWHM}(\text{Mg II})^{1.51 \pm 0.49}$ .

Previously, researchers have feared that the substantial contamination of the Mg II region by Fe II multiplets might introduce significant uncertainties in its linewidth measurements, such that Mg II-based  $M_{\text{BH}}$  estimates may not be as accurate as those based on H $\beta$ . With the recent availability of a more refined UV Fe II template (Tsuzuki et al. 2006; cf. Vestergaard & Wilkes 2001), we have higher confidence that the linewidth measurements of Mg II are reasonably robust. Our work suggests that we can measure Mg II FWHM typically to within an uncertainty of  $\sim 20\%$ . Nevertheless, it would be highly desirable to attempt to further improve the methodology for Fe II subtraction, not only in the UV but also at optical wavelengths.

#### 4.3. Comparison with Previous Studies

As shown in Section 3 (see Figure 5), our Mg II- and H $\beta$ -based  $M_{\text{BH}}$  formalisms show, in addition to somewhat improved internal scatter, subtle but systematic deviations from some of the commonly used  $M_{\text{BH}}$  estimators in the literature. In general, the formalism prescribed by our Scheme 4 (Equation (10);  $M_{\text{BH}} \propto \text{FWHM}^{1.51 \pm 0.49}$ ) gives progressively higher and lower  $M_{\text{BH}}$

values toward the low- and high-mass ends, respectively. The only exception is the H $\beta$ -based formalism of Collin et al. (2006), which gives roughly consistent results as ours over a relatively large mass range. The discrepancies between previous mass estimators and ours arise from one, or a combination, of the following factors incorporated into our analysis. (1) We use the most recently recalibrated and updated RM  $M_{\text{BH}}$  measurements from the literature (Peterson et al. 2004; Denney et al. 2006, 2009b; Metzroth et al. 2006; Bentz et al. 2007; Grier et al. 2008). (2) Our new formalism (Scheme 4, Equation(10)) uses the best-fitting value of  $\gamma$  instead of the canonical value of  $\gamma = 2$ . (3) For Mg II, we determine the scaling factor (incorporated into the coefficient  $a$  of Equation(9)) and the power-law index ( $\beta$ ) of the  $R_{\text{Mg II}}-\text{L}$  relation by fitting Equation(9) to the data, instead of simply using the existing  $R_{\text{H}\beta}-\text{L}$  relation as a surrogate. (4) Differences in the line-fitting and determination of the FWHM. We discuss each of these factors in detail below.

Specifically, assuming the canonical value of  $\gamma = 2$  in Equation(9) would, compared to our Scheme 4, underestimate  $M_{\text{BH}}$  at the low-end and overestimate  $M_{\text{BH}}$  at the high-end, for both Mg II and H $\beta$ . This accounts for most of the deviations from Vestergaard & Peterson (2006) and Kollmeier et al. (2006), and partially from others in Figure 5. In order to account for systematic biases with respect to RM-based  $M_{\text{BH}}$ , Collin et al. (2006) introduced a correction factor, which is dependent on H $\beta$  FWHM, into their H $\beta$ -based formalism assuming  $\gamma = 2$ . This correction has a similar effect as fitting  $\gamma$  as a free parameter, as we do here, and thus the rough consistency between our results and theirs is not surprising. Factor (3) is also partially responsible for producing the deviations from some of the previous Mg II-based  $M_{\text{BH}}$  estimators, such as those of McLure & Dunlop (2004) and Salviander et al. (2007), who assumed that both Mg II and H $\beta$  obey the same  $R-\text{L}$  relation, and of Kollmeier et al. (2006), who used a very steep relation of  $R_{\text{Mg II}} \propto L^{0.88}$ .

There have been previous reports of discrepancies between Mg II- and H $\beta$ -based estimators, which are sometimes claimed to correlate with luminosity or Eddington ratio (e.g., Kollmeier et al. 2006; Onken & Kollmeier 2008). These effects can be traced, at least partially, to the one-to-one relation assumed between FWHM(Mg II) and FWHM(H $\beta$ ), which is contradictory to the nonlinear relation found in this work. In fact, by adopting a nonlinear FWHM(Mg II)–FWHM(H $\beta$ ) relation and  $R_{\text{Mg II}} \propto L^{0.5}$ , our new Mg II- and H $\beta$ -based estimators yield mutually consistent results for the SDSS sample (Figure 5, panel c). We verified that the previously claimed correlations of the residuals of the Mg II- and H $\beta$ -based estimators with luminosity or Eddington ratio largely vanish; a Spearman rank analysis indicates a chance probability of 0.09 for the former and 0.05 for the latter.

It is generally accepted that the width of the variable part of the line, the line dispersion  $\sigma_{\text{line}}$  measured in the rms spectrum, is by far the best tracer of the virial velocity of the BLR gas responsible for the variable portion of the emission line (e.g., Onken & Peterson 2002), such that  $M_{\text{BH}} \propto \sigma_{\text{line}}^2$  according to the virial theorem. If the virial velocity is estimated using FWHM (or

any other measure of the linewidth) in single-epoch spectra, as long as its relation with  $\sigma_{\text{line}}$  is nonlinear,  $\gamma$  in Equation (9) is expected to deviate from  $\gamma = 2$ . This is exactly what we find in this work for FWHM(Mg II) at  $1\sigma$  significance level, as well as for FWHM(H $\beta$ ) at  $6\sigma$  significance level. In fact, the fitted value of  $\gamma = 1.51 \pm 0.49$  for Mg II (Equation (10)) and  $1.09 \pm 0.23$  for H $\beta$  (Equation (11)) are almost identical to those derived from the fitted  $\sigma_{\text{line}}\text{--FWHM}(\text{Mg II})$  and  $\sigma_{\text{line}}\text{--FWHM}(\text{H}\beta)$  relations, which have slopes of  $1.70 \pm 0.42$  and  $1.08 \pm 0.16$ , respectively. Factor (3) is justified by the compelling evidence presented in this work that the line-emitting locations of H $\beta$  and Mg II in the BLR are not identical. Possible physical processes underlying factors (2) and (3) are discussed in Section 4.2.

As an additional consideration, we have performed in this work refined and careful line fitting and determination of the FWHM, which may have subtle differences from previous results. These differences may also give rise to, to some extent, the systematic discrepancies between the mass relations in Figure 5 since we use our measured FWHM and luminosity data when producing the figure. For example, Salviander et al. (2007) did not subtract the narrow component of Mg II, leading to Mg II FWHM statistically smaller than ours; so the true deviations in Figure 5 (panel f) would be larger if their FWHM data were used. On the contrary, McLure & Dunlop (2004) over-subtracted the narrow component compared to ours (they considered a possible narrow component as having an upper limit of  $\text{FWHM} = 2000 \text{ km s}^{-1}$ , much larger than the  $900 \text{ km s}^{-1}$  used in our work), and their Mg II FWHM are statistically larger than ours; thus, the true deviations in Figure 5 (panel e) would be somewhat smaller if their FWHM data were used.

Finally, the appropriateness of our approach is further justified by the fact that our formalisms give  $M_{\text{BH}}$  values consistent with the RM measurements with the least systematic bias, as well as a reduced (intrinsic) scatter compared to previous formalisms (Section 3.3). Moreover, we find consistent masses between the Mg II- and H $\beta$ -based estimators. We thus conclude that our  $M_{\text{BH}}$  estimators introduce less systematic bias compared to previous formalisms. Obviously, more RM measurements (for both H $\beta$  and Mg II) are needed in order to improve the determination of the  $\sigma_{\text{line}}\text{--FWHM}$  relation, the  $R\text{--}L$  relation, and the index  $\gamma$  in the  $M_{\text{BH}} \propto \text{FWHM}^{\gamma}$  relation.

## 5. Summary and Conclusions

We investigate the relation between the velocity widths for the broad Mg II and H $\beta$  emission lines, derived from FWHM measurements of single-epoch spectra from a homogeneous sample of 495 SDSS Seyfert 1s and QSOs at  $0.45 < z < 0.75$ . Careful attention is devoted to accurate spectral decomposition, especially in the treatment of narrow-line blending and Fe II contamination. We find that Mg II FWHM is systematic smaller than H $\beta$  FWHM, such that  $\text{FWHM}(\text{Mg II}) \propto \text{FWHM}(\text{H}\beta)^{0.81 \pm 0.02}$ . Using 29 AGNs that have optical RM data and usable archival UV spectra, we then investigate

the relation between single-epoch Mg II FWHM and rms H $\beta$   $\sigma_{\text{line}}$  (line dispersion), a quantity regarded as a good tracer of the virial velocity of the BLR clouds emitting the variable H $\beta$  component. We find that, similar to the situation for the FWHM of single-epoch H $\beta$ , single-epoch Mg II FWHM is unlikely to be linearly proportional to rms H $\beta$   $\sigma_{\text{line}}$ . The above two findings suggest that a major assumption of previous Mg II-based virial BH mass formalisms—that the Mg II-emitting region is identical to that of H $\beta$ —is problematic. This finding and the recent updates of the reverberation-mapped BH masses (Peterson et al. 2004; Denney et al. 2006, 2009b; Metzroth et al. 2006; Bentz et al. 2007; Grier et al. 2008) motivated us to recalibrate the  $M_{\text{BH}}$  estimator based on single-epoch Mg II spectra.

Starting with the empirically well-motivated BLR radius–luminosity relation and the virial theorem,  $M_{\text{BH}} \propto L^\beta \text{FWHM}^\gamma$ , we fit the reverberation-mapped objects in a variety of different ways to constrain  $\beta$  and  $\gamma$ . For all the strategies we have considered,  $\beta$  has a well-defined value of  $\sim 0.5$ , in excellent agreement with the latest BLR radius–luminosity relation (Bentz et al. 2006, 2009), whereas  $\gamma \approx 1.5 \pm 0.5$ , which is marginally in conflict with the canonical value of  $\gamma = 2$  normally assumed in past studies. Performing a similar exercise for H $\beta$  yields  $M_{\text{BH}} \propto L^{0.5} \text{FWHM}(\text{H}\beta)^{1.09 \pm 0.22}$ , which again significantly departs from the functional forms used in the literature. The  $1\sigma$  uncertainty (scatter) is of the order of 0.3 dex relative to the RM-based masses for the H $\beta$  estimator, and  $\sim 0.4$  dex for the Mg II estimator. Using the same data set, the scatter of our H $\beta$  mass scaling relation is reduced by 0.1 dex over that of Vestergaard & Peterson (2006), indicating improvement in the internal scatter.

We use the SDSS database to compare our new  $M_{\text{BH}}$  estimators with various existing formalisms based on single-epoch H $\beta$  and Mg II spectra. BH masses derived from our Mg II-based mass estimator show subtle but important deviations from many of the commonly used  $M_{\text{BH}}$  estimators in the literature. Most of the differences stem from the recent recalibration of the masses derived from RM. Researchers should exercise caution in selecting the most up-to-date  $M_{\text{BH}}$  estimators, which are presented here.

We thank the referee, Michael Strauss, for his careful comments and helpful suggestions that improved the paper. This work is supported by Chinese NSF grants NSF-10533050 and NSF-10703006, National Basic Research Program of China (973 Program 2009CB824800) and a CAS Knowledge Innovation Program (grant no. KJCX2-YW-T05). The research of L.C.H. is supported by the Carnegie Institution for Science. Funding for the SDSS and SDSS-II has been provided by the Alfred P. Sloan Foundation, the Participating Institutions, the National Science Foundation, the U.S. Department of Energy, the National Aeronautics and Space Administration, the Japanese Monbukagakusho, the Max Planck Society, and the Higher Education Funding Council for England. The SDSS Web Site is <http://www.sdss.org/>.

## REFERENCES

Adelman-McCarthy, J. K., et al. 2007, *ApJS*, 172, 634

Akritas, M. G., & Bershady, M. A. 1996, *ApJ*, 470, 706

Bentz, M. C., Peterson, B. M., Netzer, H., Pogge, R. W., & Vestergaard, M. 2009, *ApJ*, 697, 160

Bentz, M. C., Peterson, B. M., Pogge, R. W., Vestergaard, M., & Onken, C. A. 2006, *ApJ*, 644, 133

Bentz, M. C., et al. 2007, *ApJ*, 662, 205

Chen, K., & Halpern, J. P. 1989, *ApJ*, 344, 115

Clavel, J., et al. 1991, *ApJ*, 366, 64

Collin, S., Kawaguchi, T., Peterson, B. M., & Vestergaard, M. 2006, *A&A*, 456, 75

Corbett, E. A., et al. 2003, *MNRAS*, 343, 705

Denney, K. D., Peterson, B. M., Dietrich, M., Vestergaard, M., & Bentz, M. C. 2009a, *ApJ*, 692, 246

Denney, K. D., et al. 2006, *ApJ*, 653, 152

Denney, K. D., et al. 2009b, *ApJ*, 702, 1353

Dietrich, M., Appenzeller, I., Vestergaard, M., & Wagner, S. J. 2002, *ApJ*, 564, 581

Dietrich, M., & Hamann, F. 2004, *ApJ*, 611, 761

Dietrich, M., & Kollatschny, W. 1995, *A&A*, 303, 405

Dong, X.-B., Wang, T.-G., Wang, J.-G., Fan, X., Wang, H., Zhou, H., & Yuan, W. 2009a, *ApJ*, 703, L1

Dong, X.-B., Wang, J.-G., Wang, T.-G., Wang, H., Fan, X., Zhou, H., & Yuan, W. 2009b, *ApJ* submitted (arXiv:0903.5020)

Dong, X.-B., Wang, T.-G., Wang, J.-G., Yuan, W., Zhou, H., Dai, H., & Zhang, K. 2008, *MNRAS*, 383, 581

Dong, X.-B., Zhou, H.-Y., Wang, T.-G., Wang, J.-X., Li, C., & Zhou, Y.-Y. 2005, *ApJ*, 620, 629

Ferland, G. J., Korista, K. T., Verner, D. A., Ferguson, J. W., Kingdon, J. B., & Verner, E. M. 1998, PASP, 110, 761

Ferrarese, L., & Merritt, D. 2000, ApJ, 539, L9

Ferrarese, L., Pogge, R. W., Peterson, B. M., Merritt, D., Wandel, A., & Joseph, C. L. 2001, ApJ, 555, L79

Fitzpatrick, E. L. 1999, PASP, 111, 63

Gebhardt, K., et al. 2000a, ApJ, 539, L13

Gebhardt, K., et al. 2000b, ApJ, 543, L5

Greene, J. E., & Ho, L. C. 2005, ApJ, 630, 122

Greene, J. E., & Ho, L. C. 2006, ApJ, 641, L21

Grier, C. J., et al. 2008, ApJ, 688, 837

Ho, L. C., Darling, J., & Greene, J. E. 2008, ApJ, 681, 128

Hu, C., Wang, J.-M., Ho, L. C., Chen, Y.-M., Zhang, H.-T., Bian, W.-H., & Xue, S.-J. 2008, ApJ, 687, 78

Jefferys, W. H. 1980, AJ, 85, 177

Jefferys, W. H. 1981, AJ, 86, 149

Kaspi, S., Brandt, W. N., Maoz, D., Netzer, H., Schneider, D. P., & Shemmer, O. 2007, ApJ, 659, 997

Kaspi, S., Maoz, D., Netzer, H., Peterson, B. M., Vestergaard, M., & Jannuzi, B. T. 2005, ApJ, 629, 61

Kaspi, S., Smith, P. S., Netzer, H., Maoz, D., Jannuzi, B. T., & Giveon, U. 2000, ApJ, 533, 631

Kelly, B. C. 2007, ApJ, 665, 1489

Kelly, B. C., Vestergaard, M., & Fan, X. 2009, ApJ, 692, 1388

Kim, M., Ho, L. C., Peng, C. Y., Barth, A. J., Im, M., Martini, P., & Nelson, C. H. 2008, ApJ, 687, 767

Kollmeier, J. A., et al. 2006, ApJ, 648, 128

Laor, A., Bahcall, J. N., Jannuzzi, B. T., Schneider, D. P., Green, R. F., & Hartig, G. F. 1994, ApJ, 420, 110

Laor, A., Jannuzzi, B. T., Green, R. F., & Boroson, T. A. 1997, ApJ, 489, 656

Marconi, A., Axon, D. J., Maiolino, R., Nagao, T., Pastorini, G., Pietrini, P., Robinson, A., & Torricelli, G. 2008, ApJ, 678, 693

Marconi, A., Axon, D. J., Maiolino, R., Nagao, T., Pietrini, P., Risaliti, G., Robinson, A., & Torricelli, G. 2009, ApJ, 698, L103

Markwardt, C. B. 2009, in ASP Conf. Ser. 411, Astronomical Data Analysis Software and Systems XVIII, ed. D. A. Bohlender, Daniel Durand, and Patrick Dowler (San Francisco, CA: ASP), 251

Marziani, P., & Sulentic, J. W. 1993, ApJ, 409, 612

Marziani, P., Sulentic, J. W., & Dultzin, D. 2008, RevMexAA, 32, 69

McArthur, B., Jefferys, W., & McCartney, J. 1994, BAAS, 26, 900

McGill, K. L., Woo, J.-H., Treu, T., & Malkan, M. A. 2008, ApJ, 673, 703

McLure, R. J., & Dunlop, J. S. 2004, MNRAS, 352, 1390

McLure, R. J., & Jarvis, M. J. 2002, MNRAS, 337, 109

Metzroth, K. G., Onken, C. A., & Peterson, B. M. 2006, ApJ, 647, 901

Nelson, C. H., Green, R. F., Bower, G., Gebhardt, K., & Weistroop, D. 2004, ApJ, 615, 652

Onken, C. A., Ferrarese, L., Merritt, D., Peterson, B. M., Pogge, R. W., Vestergaard, M., & Wandel, A. 2004, ApJ, 615, 645

Onken, C. A., & Kollmeier, J. A. 2008, ApJ, 689, L13

Onken, C. A., & Peterson, B. M. 2002, ApJ, 572, 746

Peterson, B. M., & Wandel, A. 1999, ApJ, 521, L95

Peterson, B. M., & Wandel, A. 2000, ApJ, 540, L13

Peterson, B. M., et al. 2004, ApJ, 613, 682

Press, W. H., Teukolsky, S. A., Vetterling, W. T., & Flannery, B. P. 1992, Numerical Recipes in FORTRAN. The Art of Scientific Computing (Cambridge: Cambridge Univ. Press)

Salviander, S., Shields, G. A., Gebhardt, K., & Bonning, E. W. 2007, ApJ, 662, 131

Schlegel, D. J., Finkbeiner, D. P., & Davis, M. 1998, ApJ, 500, 525

Shen, Y., Greene, J. E., Strauss, M. A., Richards, G. T., & Schneider, D. P. 2008, ApJ, 680, 169

Shields, J. C., Ferland, G. J., & Peterson, B. M. 1995, ApJ, 441, 507

Sulentic, J. W., Repetto, P., Stirpe, G. M., Marziani, P., Dultzin-Hacyan, D., & Calvani, M. 2006, A&A, 456, 929

Tremaine, S., et al. 2002, ApJ, 574, 740

Tsuzuki, Y., Kawara, K., Yoshii, Y., Oyabu, S., Tanabé, T., & Matsuoka, Y. 2006, ApJ, 650, 57

Vanden Berk, D. E., et al. 2001, AJ, 122, 549

van der Marel, R. P., & Franx, M. 1993, ApJ, 407, 525

Vestergaard, M. 2002, ApJ, 571, 733

Vestergaard, M., & Peterson, B. M. 2006, ApJ, 641, 689

Vestergaard, M., & Wilkes, B. J. 2001, ApJS, 134, 1

Wandel, A., Peterson, B. M., & Malkan, M. A. 1999, ApJ, 526, 579

Wang, T.-G., Dong, X.-B., Zhang, X.-G., Zhou, H.-Y., Wang, J.-X., & Lu, Y.-J. 2005, ApJ, 625, L35

Wills, B. J., Netzer, H., Brotherton, M. S., Han, M., Wills, D., Baldwin, J. A., Ferland, G. J., & Browne, I. W. A. 1993, ApJ, 410, 534

Wu, S.-M., Wang, T.-G., & Dong, X.-B. 2008, MNRAS, 389, 213

York, D. G., et al. 2000, AJ, 120, 1579

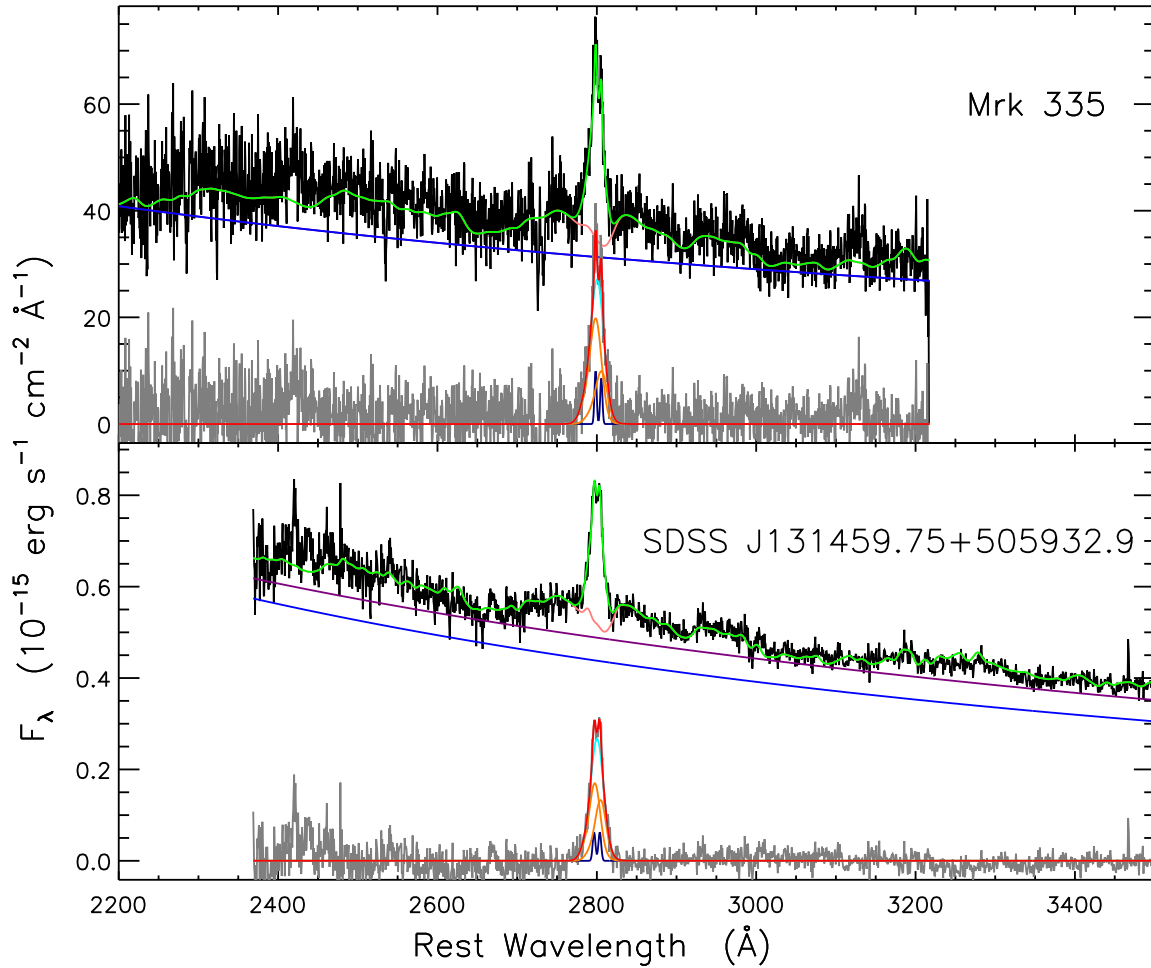


Fig. 1.— Examples of Mg II fitting for (top) the *HST* spectrum of Mrk 335 and (bottom) the SDSS spectrum of SDSS J131459.75+505932.9. The data are shown in black, the power-law AGN continuum in blue, the pseudocontinuum (power law plus Fe II emission) in pink, the final model for all fitted components in green, and the continuum-subtracted emission-line spectrum in gray. For the multi-Gaussian fit to Mg II, the narrow components are shown in navy, the individual broad components in brown, the sum of all the broad components in cyan, and the total model (narrow plus broad) in red.

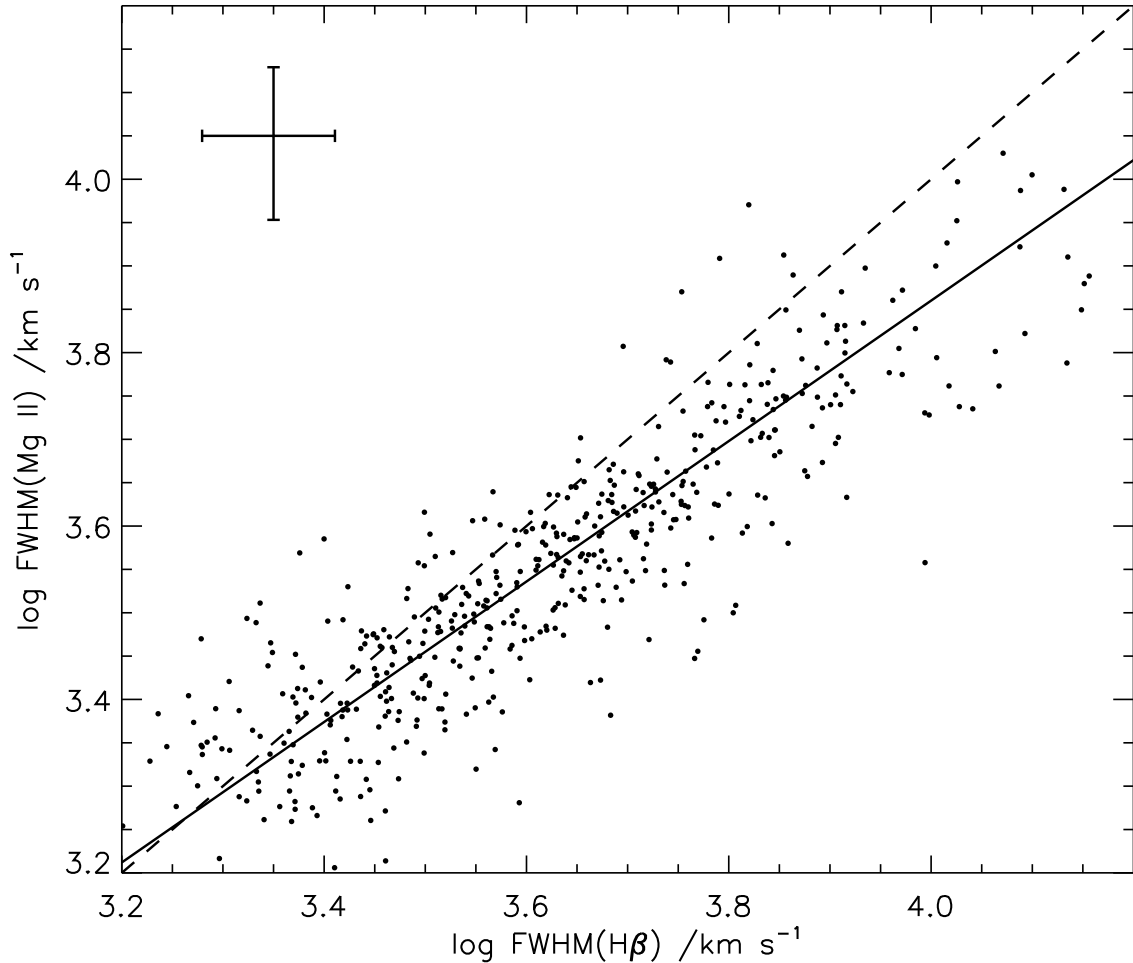


Fig. 2.— FWHM(Mg II) vs. FWHM(H $\beta$ ) for our SDSS sample. The solid line represents the best-fitting power law with index 0.81. The dashed line represents a 1:1 relationship. A typical  $1\sigma$  error bar is also shown (top-left).

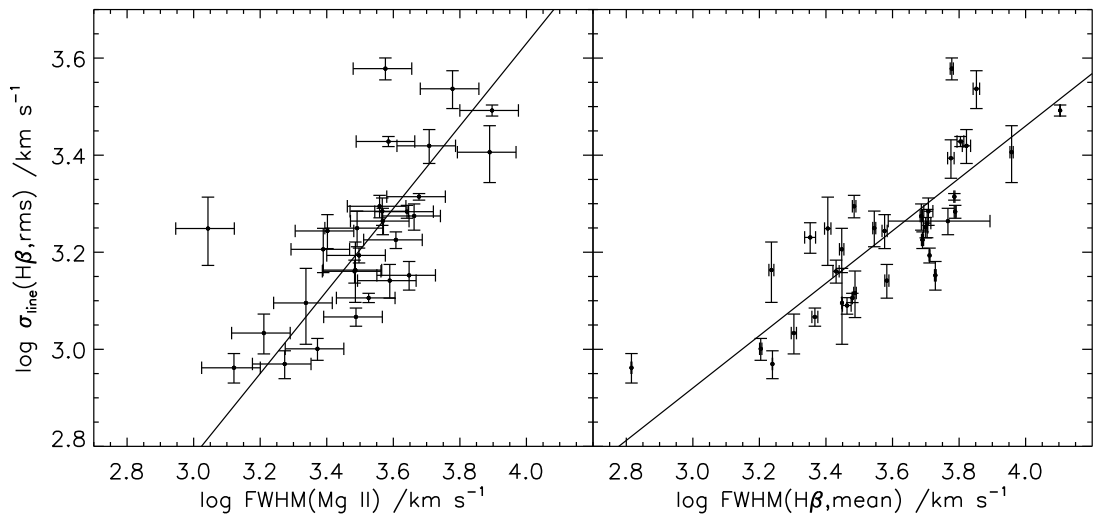


Fig. 3.—  $\sigma_{\text{line}}(\text{H}\beta, \text{rms})$  vs. FWHM(Mg II) of the 29 objects with Mg II FWHM measured in the paper (left panel) and FWHM(H $\beta$ , mean) of the 35 objects from Collin et al. (2006) and recent updated data (right panel). The solid lines show the best-fitting relations. The error bars are at 1  $\sigma$ .

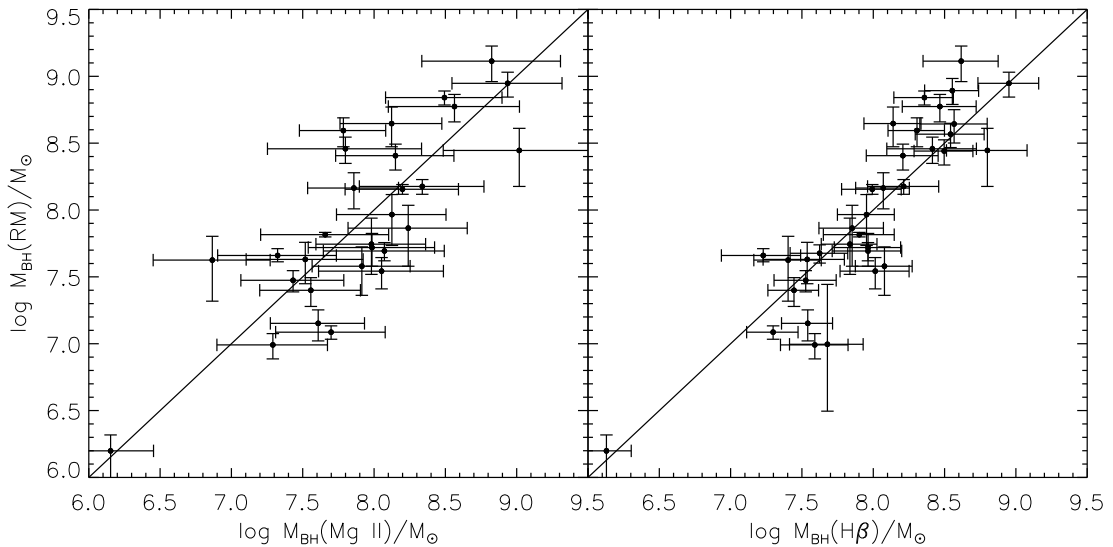


Fig. 4.— BH masses estimated from RM plotted against masses obtained from Mg II (left panel; using the 29 objects with Mg II data measured in the paper), and from  $\text{H}\beta$  (right panel; using the 35 objects from Peterson et al. (2004) and recent updated data). The solid line represents a 1:1 relationship. The error bars are at  $1\sigma$ .

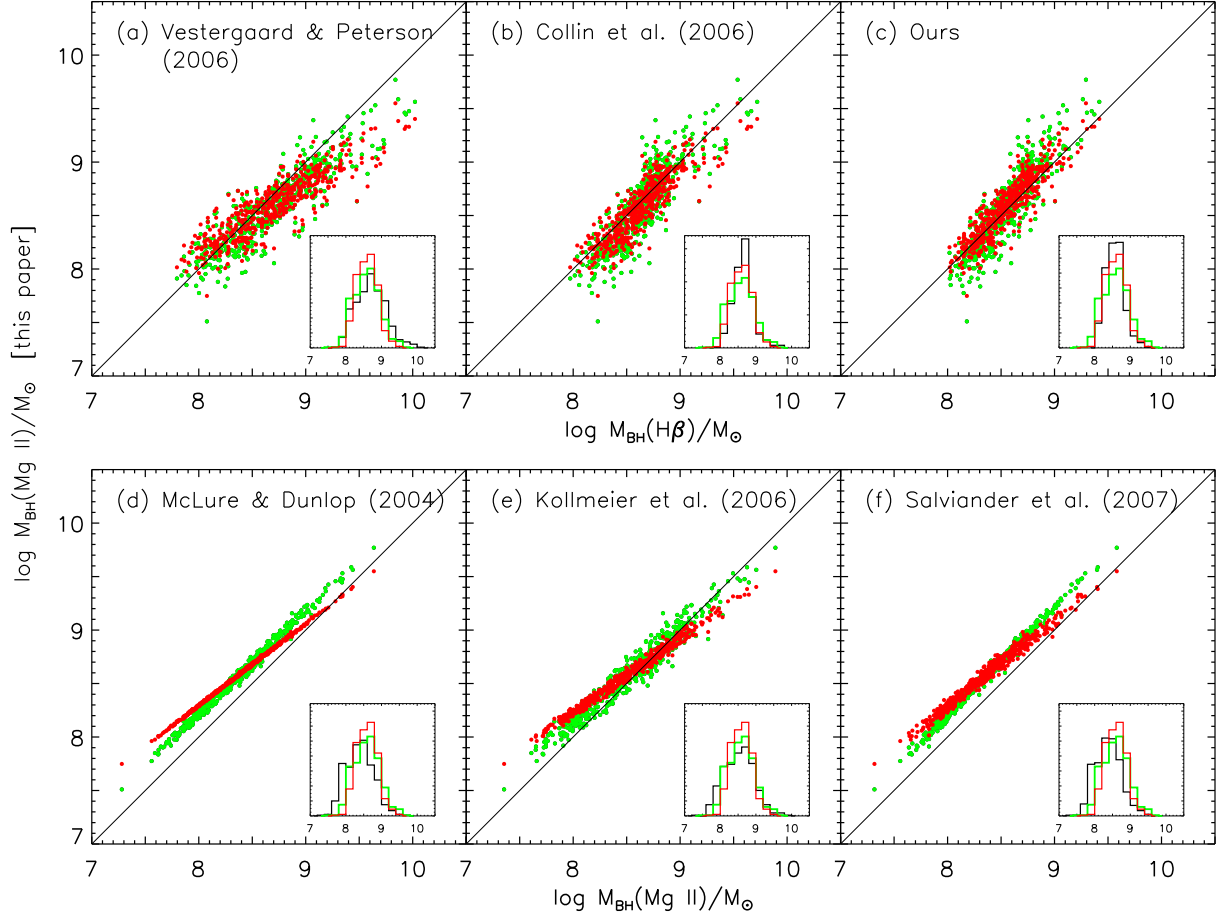


Fig. 5.— Comparison of  $M_{\text{BH}}$  estimated by our Mg II formalism with other formulae discussed in Section 3, using the SDSS sample. The y-coordinates of the green and red points represent Mg II masses estimated by Scheme 2 ( $M_{\text{BH}} \propto \text{FWHM}^2$ ) and Scheme 4 ( $M_{\text{BH}} \propto \text{FWHM}^{1.51 \pm 0.49}$ ), respectively. The inset in each panel plots the histograms of  $M_{\text{BH}}$ ; green and red lines denote the Mg II-based masses from our Schemes 2 and 4, and black lines are the comparison masses. The top three panels compare our Mg II masses with masses derived from different  $\text{H}\beta$  formalisms. The  $\text{H}\beta$  masses from Vestergaard & Peterson (2006; a) are systematically different from our Mg II masses, while those of Collin et al. (2006; b) are roughly consistent, and the best agreement comes from our newly derived formalism (Equation (9); c, red points). The bottom three panels compare our Mg II-based masses with previous Mg II-based formalisms: McLure & Dunlop (2004; d), Kollmeier et al. (2006; e), and Salviander et al. (2007; f). All show systematic deviations, mostly in the sense of giving lower masses than our formalism.

Table 1. Data for the Reverberation-mapped Sample

Name (1)	DataID (2)	$\log L_{3000}$ (erg s $^{-1}$ ) (3)	FWHM(Mg II) (km s $^{-1}$ ) (4)	$\log L_{5100}$ (erg s $^{-1}$ ) (5)	FWHM(H $\beta$ , mean) (km s $^{-1}$ ) (6)	$\sigma_{line}(H\beta, rms)$ (km s $^{-1}$ ) (7)	$\log M_{BH}(\text{RM})$ ( $10^6 M_\odot$ ) (8)
3C 120	lwp04153	44.46 $\pm$ 0.04	2780				
	lwp04500	44.37 $\pm$ 0.03	3837				
	lwp05610	44.35 $\pm$ 0.02	2568				
	lwp09048	44.41 $\pm$ 0.03	2638				
	lwp09461	44.20 $\pm$ 0.02	3411				
	lwp09850	44.22 $\pm$ 0.02	3399				
	lwp10407	44.29 $\pm$ 0.04	4083				
	lwp11524	44.28 $\pm$ 0.03	2828				
	lwp11946	44.27 $\pm$ 0.03	2786				
	lwp12536	44.36 $\pm$ 0.03	2412				
	lwr01317	43.86 $\pm$ 0.08	2874				
	lwr02983	43.73 $\pm$ 0.02	2759				
	lwr06849	44.12 $\pm$ 0.03	3997				
	lwr09102	44.34 $\pm$ 0.03	2875				
	lwr09778	43.93 $\pm$ 0.02	2735				
	lwr13786	44.30 $\pm$ 0.02	2758				
	lwr15618	44.25 $\pm$ 0.03	3040				
	lwr16609	44.17 $\pm$ 0.04	3053				
	lwr16874	44.39 $\pm$ 0.06	4431				
		<b>44.23<math>\pm</math> 0.01</b>	<b>3074</b>	44.09 $\pm$ 0.09	2327 $\pm$ 50	1166 $\pm$ 50	$55.5^{+31.4}_{-22.5}$
3C 390.3	y33y0204t	42.63 $\pm$ 0.17	7884	43.64 $\pm$ 0.14	12694 $\pm$ 13	3105 $\pm$ 81	287 $\pm$ 64
Akn 120	y29e0305t	44.48 $\pm$ 0.08	4377	43.93 $\pm$ 0.04	6143 $\pm$ 42	1921 $\pm$ 60	150 $\pm$ 19
Fairall 9	y0ya0104t	44.30 $\pm$ 0.08	3769	43.94 $\pm$ 0.10	5999 $\pm$ 66	3787 $\pm$ 196	255 $\pm$ 56
IC4329A				42.89 $\pm$ 0.15	5964 $\pm$ 134	2476 $\pm$ 226	$9.90^{+17.88}_{-11.88}$
Mrk 79	lwr01320	43.81 $\pm$ 0.02	5057				
	lwr06141	43.60 $\pm$ 0.02	4179				
		<b>43.71<math>\pm</math> 0.02</b>	<b>4597</b>	43.65 $\pm$ 0.03	4858 $\pm$ 38	1882 $\pm$ 121	52.4 $\pm$ 14.4
Mrk 110	lwp12760	43.64 $\pm$ 0.08	2216				
	lwp12761	43.82 $\pm$ 0.07	2504				
		<b>43.73<math>\pm</math> 0.05</b>	<b>2355</b>	43.66 $\pm$ 0.04	1600 $\pm$ 13	1002 $\pm$ 53	25.1 $\pm$ 6.1
Mrk 279	lwp02522	44.03 $\pm$ 0.03	4812				
	lwp10116	43.77 $\pm$ 0.02	3314				
	lwp15450	43.03 $\pm$ 0.04	5330				
	lwp15687	43.75 $\pm$ 0.02	3275				
	lwp19173	43.98 $\pm$ 0.04	3555				
	lwp19220	44.02 $\pm$ 0.03	3987				
	lwp19598	44.28 $\pm$ 0.05	3699				
	lwp19937	44.20 $\pm$ 0.04	4204				
	lwp20271	44.26 $\pm$ 0.05	4305				
	lwp20725	44.18 $\pm$ 0.03	5057				
	lwr03073	43.03 $\pm$ 0.10	3710				
	lwr10816	43.98 $\pm$ 0.04	8201				
	lwr11623	43.94 $\pm$ 0.02	6934				
	lwr15803	43.96 $\pm$ 0.03	4121				

Table 1—Continued

Name (1)	DataID (2)	$\log L_{3000}$ (erg s $^{-1}$ ) (3)	FWHM(Mg II) (km s $^{-1}$ ) (4)	$\log L_{5100}$ (erg s $^{-1}$ ) (5)	FWHM(H $\beta$ , mean) (km s $^{-1}$ ) (6)	$\sigma_{line}(\text{H}\beta, \text{rms})$ (km s $^{-1}$ ) (7)	$\log M_{\text{BH}}(\text{RM})$ ( $10^6 M_{\odot}$ ) (8)
Mrk 335	y29e0205t	<b>43.89± 0.01</b>	<b>4441</b>	43.66±0.08	5354±32	1420±96	34.9 ± 9.2
	y29e0206t	44.12± 0.04	1977				
		44.13± 0.05	1783				
Mrk 509	y0ya0305t	<b>44.13± 0.03</b>	<b>1878</b>	43.78±0.02	1735±2	933±64	14.2 ± 3.7
Mrk 590		44.55± 0.05	3357	44.16±0.10	3015±2	1276±28	143 ± 12
Mrk 817	lwr11936	44.07± 0.03	3597		43.46±0.05	2906±89	1231±49
	lwr13704	44.03± 0.04	4565				
		<b>44.05± 0.03</b>	<b>4053</b>	43.64±0.14	4899±37	1680±67	49.4 ± 7.7
NGC 3227	o5kp01010	41.76± 0.04	3688	42.48±0.04	5103±160	1925±124	42.2 ± 21.4
NGC 3516	y31r0105t	43.05± 0.02	3919				
	y31r0206t	43.23± 0.02	3775				
	y31r0306t	43.19± 0.02	3796				
	y31r0406t	42.73± 0.02	3499				
	y31r0506t	43.08± 0.02	3527				
		<b>43.06± 0.01</b>	<b>3699</b>	42.62±0.28	5840±1976	1837±115	42.7 ± 14.6
NGC 3783	o57b01010	43.39± 0.06	2524	43.02±0.06	3770±68	1753±141	29.8 ± 5.4
NGC 4051	lwp11100	41.76± 0.02	1574				
	lwp12092	41.70± 0.02	1387				
	lwp12092	41.68± 0.02	1503				
	lwp19265	41.58± 0.02	1305				
	lwp20497	41.53± 0.02	946				
	lwp23153	41.70± 0.02	918				
	lwp24347	41.81± 0.02	752				
	lwp27297	41.77± 0.02	1349				
	lwp27298	41.77± 0.02	1667				
	lwr01728	41.76± 0.02	2582				
		<b>41.68± 0.01</b>	<b>1322</b>	41.88±0.08	654±2	916±64	1.58 $^{+0.50}_{-0.65}$
NGC 4151	o42303070	43.04± 0.03	4905				
	o59701040	42.20± 0.02	3020				
		<b>42.62± 0.02</b>	<b>3849</b>	41.92±0.23	6371±150	1914±42	45.7 $^{+5.7}_{-4.7}$
NGC 4593	lwp02731	42.82± 0.02	4123				
	lwp05348	42.82± 0.02	3022				
	lwp05371	42.81± 0.02	3288				
	lwp05394	42.83± 0.02	2778				
	lwp05411	42.80± 0.02	3444				
	lwp05430	42.74± 0.02	3107				
	lwp06266	42.64± 0.02	3237				
	lwp06300	42.72± 0.02	3033				
	lwp12278	43.01± 0.02	2822				
	lwp12279	43.03± 0.02	5194				
	lwr07884	42.83± 0.02	2723				
	lwr09818	42.77± 0.02	1929				
	lwr10539	42.86± 0.02	2987				

Table 1—Continued

Name (1)	DataID (2)	$\log L_{3000}$ (erg s $^{-1}$ ) (3)	FWHM(Mg II) (km s $^{-1}$ ) (4)	$\log L_{5100}$ (erg s $^{-1}$ ) (5)	FWHM(H $\beta$ , mean) (km s $^{-1}$ ) (6)	$\sigma_{line}(\text{H}\beta, \text{rms})$ (km s $^{-1}$ ) (7)	$\log M_{\text{BH}}(\text{RM})$ ( $10^6 M_{\odot}$ ) (8)
	lwr10622	42.81± 0.02	3117				
	lwr16177	42.87± 0.02	3321				
		<b>42.82± 0.01</b>	<b>3140</b>	42.85± 0.04	5143± 16	1561± 55	9.8± 2.1
NGC 5548	y0ya0205t	43.01± 0.03	4756	43.31± 0.02	6107± 23	2063± 32	$65.4^{+2.6}_{-2.5}$
NGC 7469	y3b6010bt	43.67± 0.03	3061	43.30± 0.05	1722± 30	1456± 207	12.2± 1.4
PG 0026+129	y2jk0108t	45.18± 0.04	1104	44.95± 0.08	2544± 56	1774± 285	393± 96
PG 0052+251				44.78± 0.12	5008± 73	1783± 86	369± 76
PG 0804+761	lwr13645	45.14± 0.02	5175				
	lwr16666	44.93± 0.12	2533				
		<b>45.04± 0.06</b>	<b>3621</b>	44.88± 0.09	3053± 38	1971± 105	693± 83
PG 0844+349	y0p80105t	44.53± 0.04	3045	44.19± 0.07	2694± 58	1448± 79	92.4± 38.1
PG 0953+414				45.15± 0.07	3071± 27	1306± 144	276± 59
PG 1211+143	y0iz0403t	44.81± 0.03	1610				
	y0iz0404t	44.82± 0.03	1642				
		<b>44.82± 0.02</b>	<b>1626</b>	44.70± 0.08	2012± 37	1080± 102	146± 44
PG 1226+023	y0g4020et	46.08± 0.06	3420				
	y0g4020ft	45.98± 0.06	3105				
	y0g4020ht	46.20± 0.09	2900				
	y0g4020jt	46.24± 0.08	2839				
	y0g4020lt	46.24± 0.07	3032				
	y0g4020nt	46.24± 0.07	3022				
	y0nb0104t	45.94± 0.06	3422				
		<b>46.13± 0.03</b>	<b>3098</b>	45.93± 0.06	3509± 36	1777± 150	886± 187
PG 1229+204	lwr13136	44.41± 0.07	3054				
	lwr16071	44.47± 0.03	4940				
		<b>44.44± 0.04</b>	<b>3884</b>	43.65± 0.06	3828± 54	1385± 111	73.2± 35.2
PG 1307+085				44.82± 0.05	5059± 133	1820± 122	440± 123
PG 1411+442	o65617010	44.81± 0.03	2452	44.52± 0.05	2801± 43	1607± 168	443± 146
PG 1426+015	lwp05440	45.14± 0.03	6957				
	lwp05446	45.04± 0.06	4575				
	lwr16020	44.92± 0.07	6776				
		<b>45.04± 0.03</b>	<b>5997</b>	44.60± 0.09	7113± 160	3442± 308	1298± 385
PG 1613+658	lwp19372	45.09± 0.03	7518				
	lwp19380	45.10± 0.03	7996				
		<b>45.09± 0.02</b>	<b>7753</b>	44.73± 0.10	9074± 103	2547± 342	279± 129
PG 1617+175	lwp07592	44.81± 0.06	5951				
	lwp25629	44.64± 0.05	4375				
		<b>44.73± 0.04</b>	<b>5102</b>	44.36± 0.10	6641± 190	2626± 211	594± 138
PG 1700+518	lwp02520	44.60± 0.05	3042				
PG 2130+099	lwp03568	44.66± 0.08	2208				
	lwp07205	44.53± 0.03	2039				
	lwr01774	44.47± 0.06	1820				
	lwr04610	44.52± 0.03	1290				

Table 1—Continued

Name (1)	DataID (2)	$\log L_{3000}$ (erg s $^{-1}$ ) (3)	FWHM(Mg II) (km s $^{-1}$ ) (4)	$\log L_{5100}$ (erg s $^{-1}$ ) (5)	FWHM(H $\beta$ , mean) (km s $^{-1}$ ) (6)	$\sigma_{line}(\text{H}\beta, \text{rms})$ (km s $^{-1}$ ) (7)	$\log M_{\text{BH}}(\text{RM})$ ( $10^6 M_{\odot}$ ) (8)
lwr04628		$44.58 \pm 0.06$	2479				
lwr15802		$44.51 \pm 0.03$	2885				
		<b><math>44.55 \pm 0.02</math></b>	<b>2174</b>	$44.40 \pm 0.02$	$2853 \pm 39$	$1624 \pm 86$	$38 \pm 15$

Note. — Column (1) object name; Column (2) identification name of the spectrum in *IUE* (prefix “lw”) or *HST* archives; Column (3) monochromatic continuum luminosity at 3000 Å. For objects with multiple spectra, mean monochromatic continuum luminosity at 3000 Å is listed in bold at the bottom of each object. Column (4) FWHM of broad Mg II. For objects with multiple spectra, mean FWHM is listed in bold at the bottom of each object. Column (5) monochromatic continuum luminosity at 5100 Å taken from Bentz et al. (2009). For objects having multiple measurements, here listed is mean value. Column (6) H $\beta$  FWHM of mean spectra taken from Collin et al. (2006) and recent update listed in Section 3.2. For objects having multiple measurements, here listed is mean value. Column (7) H $\beta$   $\sigma_{line}$  of rms spectra taken from Peterson et al. (2004) and recent update listed in Section 3.2. For objects having multiple measurements, here listed is mean value. Column (8) BH mass from RM taken from Peterson et al. (2004) and recent update listed in Section 3.2.

**Table 2.** Continuum and Emission-line Parameters of the SDSS Sample

SDSS Name (1)	$z$ (2)	$\log L_{5100}$ (3)	FWHM(H $\beta^b$ ) (4)	$\log F(H\beta^b)$ (5)	$\log F(H\beta^n)$ (6)	$\log L_{3000}$ (7)	FWHM(Mg II $^b$ ) (8)	$\log F(\text{Mg II}^b)$ (9)	$\log F(\text{Mg II}^n)$ (10)
J000011.96+000225.3	0.478	44.69	3037	-13.89	-15.68	44.99	3284	-13.84	-14.89
J000110.97-105247.5	0.529	44.98	6807	-13.73	-15.53	45.18	5797	-13.85	-15.15
J001725.36+141132.6	0.514	45.23	5676	-13.49	-15.52	45.49	4432	-13.64	-14.71
J002019.22-110609.2	0.492	44.85	2832	-13.74	...	45.00	2677	-13.91	-16.16
J005121.25+004521.5	0.727	45.04	2572	-14.09	-15.07	45.14	1606	-14.42	-15.41
J005441.19+000110.7	0.646	45.08	2220	-14.24	...	45.13	2172	-14.20	-15.29
J010448.57-091013.0	0.469	44.77	4610	-13.81	-15.33	44.88	2627	-14.11	-15.86
J010644.16-103410.6	0.468	44.72	3873	-13.83	-15.35	44.85	3074	-13.80	-15.43
J011132.34+133519.0	0.576	45.13	8060	-13.66	-15.72	45.39	5495	-13.73	-14.87
J012016.73-092028.8	0.495	44.71	3284	-13.72	-16.02	45.05	3312	-13.58	-16.07

Note. — Column (1) object name; Column (2) redshift derived from the peak of [O III]  $\lambda 5007$ . Column (3) luminosity of the power-law continuum at 5100 Å. Column (4) FWHM of broad H $\beta$ . Column (5) flux of the broad component of H $\beta$ . Column (6) flux of the narrow component of H $\beta$ . Column (7) luminosity of the power-law continuum at 3000 Å. Column (8) FWHM of broad Mg II. Column (9) flux of the broad component of Mg II. Column (10) flux of the narrow component of Mg II. Luminosities, fluxes, and FWHM are in units of erg s $^{-1}$ , erg s $^{-1}$  cm $^{-2}$ , and km s $^{-1}$ , respectively.(This table is available in its entirety in a machine-readable form in the online journal. A portion is shown here for guidance regarding its form and content.)

Table 3. Regression Results for

$$\log \left[ \frac{\text{FWHM(Mg II)}}{1000 \text{ km s}^{-1}} \right] = k \log \left[ \frac{\text{FWHM(H}\beta\text{)}}{1000 \text{ km s}^{-1}} \right] + c$$

Method	$k$	$c$
OLS	$0.73 \pm 0.02$	$0.09 \pm 0.01$
WLS	$0.73 \pm 0.02$	$0.09 \pm 0.01$
FITexy	$0.77 \pm 0.01$	$0.06 \pm 0.02$
FITexy_T02	$0.81 \pm 0.03$	$0.04 \pm 0.02$
Gaussfit	$0.81 \pm 0.03$	$0.04 \pm 0.02$
BCES (bisector)	$0.78 \pm 0.03$	$0.06 \pm 0.02$
BCES (orthogonal)	$0.81 \pm 0.02$	$0.05 \pm 0.01$
LINMIX_ERR	$0.79 \pm 0.03$	$0.05 \pm 0.02$

Table 4. Regression Results for  $\log \left[ \frac{M_{\text{BH(RM)}}}{10^6 M_{\odot}} \right] = a + \beta \log \left( \frac{L_{3000}}{10^{44} \text{ erg s}^{-1}} \right) + \gamma \log \left[ \frac{\text{FWHM(Mg II)}}{1000 \text{ km s}^{-1}} \right]$  and  $M_{\text{BH}}$  Comparisons

Scheme	$a$	$\beta$	$\gamma$	$\Delta M_{\text{BH}}(\text{RM})$		$\Delta M_{\text{BH}}(\text{H}\beta)$		$\Delta M_{\text{BH}}(\text{H}\beta)$		$\Delta M_{\text{BH}}(\text{H}\beta)$		
				(Vestergaard+06)		(Collin+06)		(Ours)		(Ours)		
	(1)	(2)	(3)	(4)	Mean	$1\sigma$	Mean	$1\sigma$	Mean	$1\sigma$	Mean	$1\sigma$
Scheme 1 <sup>a</sup>	$1.15 \pm 0.27$	$0.46 \pm 0.08$	$1.48 \pm 0.49$		0.01	0.39	0.15	0.22	0.10	0.14	0.07	0.12
Scheme 2	$0.88 \pm 0.08$	$0.48 \pm 0.08$	2		0.01	0.42	0.11	0.19	0.06	0.18	0.03	0.18
Scheme 3	$1.03 \pm 0.08$	$0.48 \pm 0.08$	1.70		0.01	0.40	0.13	0.20	0.07	0.15	0.05	0.14
Scheme 4	$1.13 \pm 0.27$	0.5	$1.51 \pm 0.49$		0.01	0.40	0.10	0.21	0.05	0.14	0.03	0.12

Note. — Fits for the 29 objects with Mg II data measured in the paper.  $\Delta M_{\text{BH}} \equiv \log M_{\text{BH}} - \log M_{\text{BH}}(\text{Mg II})$  are the differences of the masses obtained from different methods with masses estimated by our Mg II formalism for each scheme. Column (5) The mean and standard deviation of the deviations between BH masses obtained from RM and our single-epoch Mg II estimators. The mean and standard deviation of the deviations between masses estimated from our single-epoch Mg II estimator and masses derived using (Column 6) the H $\beta$  formalism of Vestergaard & Peterson (2006), (Column 7) the H $\beta$  formalism of Collin et al. (2006), and (Column 8) the new H $\beta$  formalism obtained in this work (Equation (11)) for the SDSS sample.

<sup>a</sup>Scheme 1 is fitted by using the code MLINMIX\_ERR of Kelly (2007).